Semnan University

Journal of Modeling & Simulation in Electrical & Electronics Engineering (MSEEE)

Journal homepage: **https://mseee.semnan.ac.ir/**

ISSN: 2821-0786

Improving Photovoltaic Performance by Tuning Interface Band Alignment in CBTS/CH3NH3PBI3/ZnO Perovskite Solar Cells

Ali Ghasemi Koosheh*[1], Seyed Mohammad Sadeghzadeh[1], Iman Gharibshahian[2] and Reza Keypour[2]

***Abstract*-- This work presents a novel $CH_3NH_3PbI_3$-based perovskite solar cell structure with low-cost and widely available Cu_2BaSnS_4 (CBTS) and ZnO materials as charge transport layers (CTLs). A comprehensive analysis was conducted on the performance of the standard $CH_3NH_3PbI_3$ cell, which comprises FTO/TiO_2/$CH_3NH_3PbI_3$/Spiro-OMeTAD/Au structure, and the suggested structure of FTO/ZnO/$CH_3NH_3PbI_3$/CBTS/Ni. We evaluated the characteristics of perovskite cells (PCs) by assessing the effect of the bulk defect density of the $CH_3NH_3PbI_3$ layer and the thicknesses of different layers. Moreover, we examined the impact of interface defects at the CTLs/$CH_3NH_3PbI_3$ interfaces. The thickness and defect of the $CH_3NH_3PbI_3$ layer are fine-tuned to 900 nm and 7×10^{13} cm^{-3}, respectively, resulting in an optimized efficiency of 26.38%. This research demonstrates that incorporating CBTS as a positive charge-transport layer (PCTL) and ZnO as a negative charge transport layer significantly enhances J_{sc} by establishing proper band alignment with the $CH_3NH_3PbI_3$ absorber. This enhancement improves cell efficiency by reducing interface carrier recombination. Finally, we assessed the variation of operating temperature, cell parasitic resistances, and rear electrode work function on the efficiency. These results suggest that CBTS and ZnO materials have the potential to serve as CTLs for the production of economical, exceptionally effective solar devices based on $CH_3NH_3PbI_3$ material.**

***Keywords* — $CH_3NH_3PbI_3$ perovskite solar cell, Charge transport layer, Cu_2BaSnS_4, ZnO, Efficiency.**

I. Introduction

Today, there is a growing focus on technologies powered by renewable energies, as the use of fossil fuels continues to pollute the environment and contribute to climate change. One of the best and cleanest renewable energy sources is solar energy, which has been exploited in various ways over the past few decades [1,2]. One of the most popular and efficient ways to harness solar energy is through solar cells. Silicon-based cells are among the best-known and most common solar cells; however, manufacturing them at very high temperatures is a challenge [3].

In recent times, perovskite cells (PCs) have gained significant attention due to their exceptional electronic and optical characteristics, which have facilitated their large-scale production at relatively low cost. Its high flexibility makes it a versatile material that can be easily adapted for different applications. It is considered an alternative material for silicon [4]. Lately, there has been a significant advancement in PCs efficiency, which has now reached an impressive 26.1%, and in this regard, these cells can compete with silicon cells [5]. The naturally occurring perovskite compound, $CaTiO_3$, serves as a model for producing synthetic perovskite materials, ABX_3,

Received; 2025-12-21 Revised; 2026-05-05 Accepted; 2026-05-13

1.Department of Power Electrical Engineering, Faculty of Engineering, Shahed University, Tehran, Iran.
2.Faculty of Electrical and Computer Engineering, Semnan University, Semnan, Iran.
*Corresponding author: ali.ghasemikousheh@shahed.ac.ir

Cite this article as:
Ghasemi Koosheh, A., Sadeghzadeh, S, M., Gharibshahian, I. & Keypour, R. (2026). Improving Photovoltaic Performance by Tuning Interface Band Alignment in CBTS/CH3NH3PBI3/ZnO Perovskite Solar Cells. *Journal of Modeling & Simulation in Electrical & Electronics Engineering (MSEEE)*. Semnan University Press. 6 (3), 19-35.
DOI: https://doi.org/10.22075/MSEEE.2026.40126.1243

which are utilized in the manufacturing of solar cells. A is a large positive ion, B is a small positive ion, and X is a halogen negative ion. From 2009 to 2016, perovskite cells were made with an absorber layer of CH_3NH_3PbX, where X is either Br, I, or Cl [6].

In perovskite cell structures, TiO_2 is among the most frequently used materials as the negative charge-transport layer (NCTL). The need for high-temperature annealing, at 500 °C, is one of the drawbacks of this material [7]. In addition, TiO_2 exhibits low electron mobility and is susceptible to degradation by UV radiation [8]. Zinc Oxide (ZnO) has been identified as a promising and effective alternative to conventional NCTLs, demonstrating excellent PC efficiency as reported by Pandey et al. in 2021 [9]. This material has shown great potential to enhance the performance of perovskite solar cells, making it a noteworthy alternative for NCTLs. Also, Liu and Smith achieved an efficiency of 15.7% by employing a low-temperature solubility-based procedure [10]. These reports and studies show that ZnO can serve as a good alternative, while also enhancing the power conversion efficiency (PCE) of PCs. Another substance, zinc oxide indium gallium (IGZO), has several advantages as an NCTL, such as good electron mobility, low resistance, good optical transparency, and compatibility with low-temperature processing. In addition, IGZO can be used in a variety of ways, such as sputtering, atomic layer deposition, or solution processing, which facilitates the flexibility and scalability of the cell [11,12].

The conventional perovskite cells face issues with the organic Spiro-OMeTAD as a PCTL, requiring doping also additives such as Hygroscopic LiTFSI salt. These factors contribute to the instability of perovskite cells.

A substantial portion, approximately 33.9% of the total cell costs, is allocated to the Spiro-OMeTAD PCTL compound and the Au electrode, typically employed as the back metal electrode layer [13]. In the search for a suitable replacement for Spiro-OMeTAD that is both weather-resistant and stable, copper-based materials have appeared as hopeful candidates. For instance, the inorganic material Cu_2O is an excellent choice because of its desirable properties, including high hole mobility, an ultra-thin layer, and a good energy-level (EL) match with $CH_3NH_3PbI_3$ [14]. In addition, the use of suitable inorganic materials in the hole-transport layer can lower the cell cost and increase stability. Cu_2BaSnS_4 (CBTS) is another inorganic material that exhibits advantageous attributes, including high carrier mobility, high stability, and high transparency in the visible range. The CBTS exhibits excellent thermal stability, optimal conductivity, and favorable energy level alignment (ELA) with the PCs. The unique characteristics of the CBTS make it a promising candidate for enhancing the efficiency of perovskite solar cells [15].

In this study, we investigate different positive and negative charge-transport substances for PCs based on $CH_3NH_3PbI_3$ and introduce a novel photovoltaic device configuration, FTO/ZnO/$CH_3NH_3PbI_3$/CBTS/Ni, with CBTS serving as the PCTL and ZnO as the NCTL. In this particular investigation, the SCAPS-1D simulation software is employed to meticulously simulate and assess the proposed cell's overall performance. The study explores interactions among various physical parameters across layers, backside metallic functionality on electrical properties, defect density, parasitic resistances, and operating temperatures to achieve device optimization.

II. Device Arrangement and Computational Simulation

In this study, we utilized the SCAPS-1D software [16]. This software was employed to examine and model the efficiency of the photovoltaic cells. The SCAPS-1D software includes a wide range of suggested optical, electrical, and photovoltaic models, making it suitable for simulating various types of photovoltaic cells such as CIGS [17-21], polymer [22], graphene [23], dye-sensitized [24,25], perovskite [26], and Sb_2Se_3 cells [27-32].

Based on several computational studies, the software conducts numerical simulations, including the Poisson equation, hole/electron continuity equation, hole/electron charge-transport equation, and absorption coefficient equation. These simulations play a crucial role in understanding the electrical and physical properties of solar devices, aiding in the optimization of device design and performance.

Eq. 1 presents Poisson's equation, a fundamental equation in the analysis of different solar cells.

$$\frac{d^2\phi(x)}{dx^2} = \frac{q}{\varepsilon_0\varepsilon_r}\left(p(x) - n(x) + N_D - N_A + \rho_p - \rho_n\right) \tag{1}$$

The equation delineates the connection between the electrostatic potential (φ) and the diverse factors influencing it within a material. These factors include the electronic charge (q), the vacuum dielectric constant (ε_0), the relative permittivity (ε_r), and the shallow donor (N_D) and shallow acceptor (N_A) impurity densities. The term ρ_p represents the distribution density of the hole, while ρ_n signifies the distribution density of the electron. The *p(x)* and *n(x)* describe the positive and negative charge distribution, respectively, within a material, with respect to their position along the x-axis. According to Eqs. (2) and (3), the negative and positive charge continuity equations are stated as follows:

$$\frac{dj_n}{dx} = G - R \tag{2}$$

$$\frac{dj_p}{dx} = G - R \tag{3}$$

In Eqs. (2) and (3), variables j_n and j_p denote the J_{sc} associated with negative and positive charge transport. G stands for the new charge carriers' creation rate (both electrons and holes) via generation processes, while R is the rate at which charge carriers combine and disappear through recombination processes. Also, the electron and hole-charge transport equations are presented in Eqs. (4) and (5).

$$j_n = D_n \frac{dn}{dx} + \mu_n n \frac{d\phi}{dx} \quad (4)$$

$$j_p = D_p \frac{dp}{dx} + \mu_p p \frac{d\phi}{dx} \quad (5)$$

In the aforementioned equations, D_n and D_p represent the measures of electron and hole mobilities in the material, respectively. The μ_n and μ_p describe how efficiently electrons and holes can traverse through the substance, with higher values indicating greater mobility.

Finally, the absorption coefficient of materials is obtained according to the following equation:

$$\alpha(\lambda) = (A + \frac{B}{h\nu})\sqrt{h\nu - E_g} \quad (6)$$

In this equation, A and B are fixed values, *h* stands for the Planck constant, ν denotes the incoming photon frequency, and E_g represents the energy gap in the absorber layer. The simulated $CH_3NH_3PbI_3$-based cell (FTO/NCTLs/$CH_3NH_3PbI_3$/PCTLs/Au) is shown in Fig. 1.

In this configuration, the $CH_3NH_3PbI_3$ layer is responsible for absorption, possessing an E_g of 1.5 eV. The n-type TiO_2, ZnO, and IGZO layers act as NCTLs with respective E_g of 3.2, 3.3, and 3.05 eV. Additionally, the FTO is used as a TCO layer with an E_g of 3.5 eV. These materials are used in a computational simulation to investigate their potential for implementation in solar cell applications. To increase the collection of carriers generated by light, the p^+-Spiro-OmeTAD, Cu_2O, and CBTS are introduced as PCTLs between the 0.45 μm thick intrinsic $CH_3NH_3PbI_3$ and the back metal electrode layer. In this study, we employ n-type NCTLs with a doping density of 1×10^{18} cm^{-3}, along with a 0.5-μm-thick FTO TCO layer that has a doping density of 1×10^{18} cm^{-3}. To streamline the computational process, the approximated thermal velocity of negative and positive charges in each material at a temperature of 300 K is approximately 10^7 cm/s, a common value for this parameter in similar calculations. Also, it is postulated that the recombination velocity on the surface for both the positive and negative charges, at the metal contacts located at the front and back, is 10^7 cm/s. Table I provides details about the parameters for all layers utilized in the solar cell simulation, while Table II presents information on the defect density at the NCTL/$CH_3NH_3PbI_3$ and $CH_3NH_3PbI_3$/PCTL interfaces. The data were recorded at a temperature of 300 K, and the light intensity was AM.1.5 (1000 W/m^2).

It should be noted that the SCAPS simulation provides an idealized description of device operation. The model assumes smooth interfaces and uniform material properties and does not account for several non-ideal effects such as interface roughness, grain boundary recombination, ion migration, and optical reflection or scattering losses, which may occur in practical devices. As a result, the simulated efficiency represents a theoretical upper limit for high-quality films under ideal conditions. Nevertheless, the results offer valuable insights into how band alignment, defect reduction, and transport-layer optimization can guide the design of efficient and stable perovskite solar cells in experimental practice.

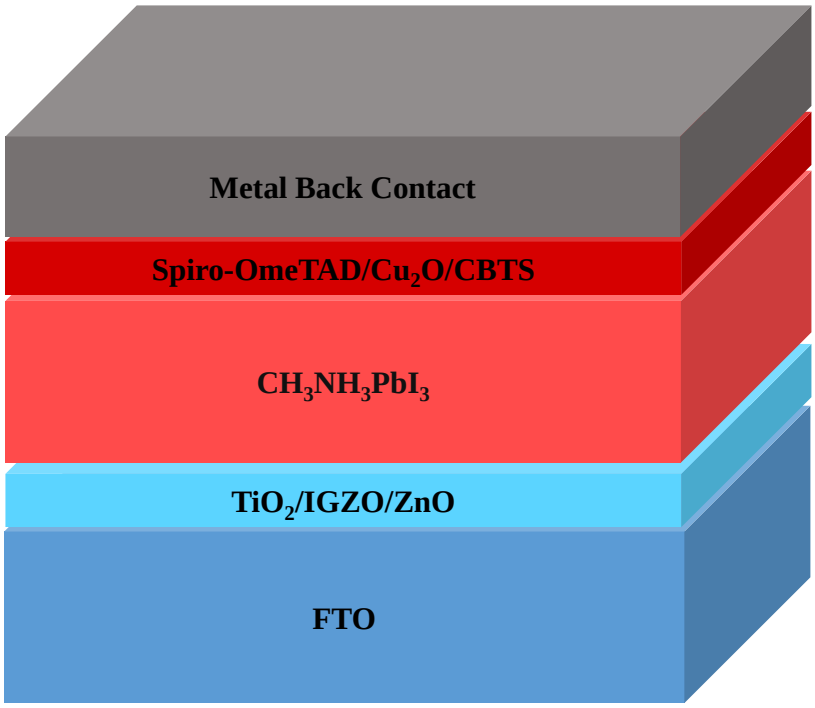

Fig. 1. Structure of the FTO/NCTLs/$CH_3NH_3PbI_3$/PCTLs cell.

TABLE I
Input Data Used for Perovskite Solar Cell Simulation [4,6,11-15].

Parameters/Materials	FTO	ZnO	IGZO	TiO_2	$CH_3NH_3PbI_3$	Spiro	CBTS	Cu_2O
Thickness (nm)	500	variable	variable	variable	450	variable	variable	variable
E_g (eV)	3.5	3.3	3.05	3.2	1.5	3	1.9	2.17
χ (eV)	4	4	4.16	4	3.93	2.45	3.6	3.2
ε_r	9	9	10	9	30	3	5.4	7.1
N_c (1/cm^3)	2.2×10^{18}	3.7×10^{18}	5×10^{18}	2×10^{18}	2.2×10^{18}	2.2×10^{18}	2.2×10^{18}	2.2×10^{18}
N_v (1/cm^3)	1.8×10^{19}	1.8×10^{19}	5×10^{18}	1.8×10^{19}	1.8×10^{19}	1.8×10^{19}	1.8×10^{19}	1.8×10^{19}
μ_n (cm^2/Vs)	20	100	15	20	50	2×10^{-4}	30	200
μ_p (cm^2/Vs)	10	25	0.1	10	50	2×10^{-4}	10	80
N_D (1/cm^3)	2×10^{19}	1×10^{18}	1×10^{18}	1×10^{18}	-	-	-	-
N_A (1/cm^3)	-	-	-	-	-	1×10^{18}	1×10^{18}	1×10^{18}
Defect density (1/cm^3)	1×10^{18}	1×10^{15}	1×10^{15}	1×10^{15}	7×10^{13}	1×10^{15}	1×10^{15}	1×10^{15}

TABLE II
Defect Specifications of the Simulated Perovskite Solar Cell at the Interfaces [13].

Interfaces	Electron capture cross-section (cm^2)	Hole capture cross-section (cm^2)	Defect type	Trap position	Energy with respect to Reference (eV)	Trap density (1/cm^2)
NCTL/$CH_3NH_3PbI_3$	1×10^{-17}	1×10^{-18}	Single (A)	Above the VBM	0.32	1×10^{11}
$CH_3NH_3PbI_3$/PCTL	1×10^{-18}	1×10^{-19}	Single (A)	Above the VBM	0.07	1×10^{11}

III. Results and Discussion

The goal of this work is to increase efficiency and reduce cell costs. First, a cell with the configuration of FTO/NCTL/$CH_3NH_3PbI_3$/PCTL/Au is considered. Then, a comparison among the three TiO_2, ZnO, and IGZO materials is carried out to find the best material for NCTL with a focus on high efficiency and lower cost. Also, this comparison is carried out using Spiro-OMeTAD, Cu_2O, and CBTS materials as PCTLs to identify the best one. The comparison between the materials in the NCTLs and PCTLs is performed in two modes: fixed thickness and variable thickness to select the optimal layer. After selecting the optimal layers for NCTL and PCTL, the effects of some common metal-back contact materials, such as Au, Pd, Pt, Cu, Ni, and C, on cell efficiency were analyzed based on conductivity, high efficiency, and lower cost.

A. Perovskite cell performance with Spiro-OMeTAD as PCTL and the use of various materials as NCTL

In this section, the described cell features a structure that includes FTO as a transparent conductive oxide layer, which facilitates electron transfer through the electron transport layer, allowing it to absorb electron charges. The cell absorber layer is acknowledged as $CH_3NH_3PbI_3$, Spiro-OMeTAD as PCTL, and the three materials TiO_2, ZnO, and IGZO as NCTLs. Gold metal (Au) has also been applied as a metal back contact (MBC). Table I lists the parameters associated with each layer, while Table II presents information on the defect specifications among the layers.

The NCTL plays a crucial role in transferring the negative charge generated in the $CH_3NH_3PbI_3$ layer to the transparent conductive oxide (TCO) layer and then to the external circuit. TiO_2 is widely used as NCTL. However, using this material

requires a very high-temperature manufacturing process, which increases costs and creates problems for the cell. ZnO is another material that can replace TiO_2 [33,34], as it does not need a high-temperature manufacturing process. It has been used in the solar cell field for several years, and it also improves cell efficiency due to its high optical and conductive properties [33,35,36]. Fig. 2 and Table III demonstrate the photovoltaic parameters of $CH_3NH_3PbI_3$ PCs with various NCTLs. In this simulation, the thickness of the NCTLs (TiO_2, ZnO, and IGZO) is fixed at 100 nm. Meanwhile, the Spiro-OMeTAD PCTL has a constant thickness of 200 nm. According to Table III and Fig. 2, the V_{oc} of cells with ZnO and TiO_2 NCTLs increases to 1.16 V, surpassing the V_{oc} value of the structure featuring an IGZO NCTL. The reason for the enhanced performance of the FTO/ZnO/$CH_3NH_3PbI_3$/Spiro-OMeTAD/Au and FTO/TiO_2/$CH_3NH_3PbI_3$/Spiro-OMeTAD/Au configurations is due to their more favorable band alignment and reduced interface recombination rates compared to the FTO/IGZO/$CH_3NH_3PbI_3$/Spiro-OMeTAD/Au structure. Fig. 2 and Table III show that J_{sc} does not change with NCTL, whereas the V_{oc} and the FF parameters are affected by it. As can be seen, the cell incorporating ZnO exhibits the highest efficiency of 21.43%.

TABLE III
Output Parameters for Different NCTLs with 100 nm Thickness.

Device arrangement	V_{oc} (V)	J_{sc} (mA/cm^2)	FF (%)	PCE (%)
FTO/TiO_2/$CH_3NH_3PbI_3$/Spiro-OMeTAD/Au	1.16	24.71	73.58	21.16
FTO/IGZO/$CH_3NH_3PbI_3$/Spiro-OMeTAD/Au	1.08	24.70	72.66	19.44
FTO/ZnO/$CH_3NH_3PbI_3$/Spiro-OMeTAD/Au	1.16	24.71	74.20	21.43

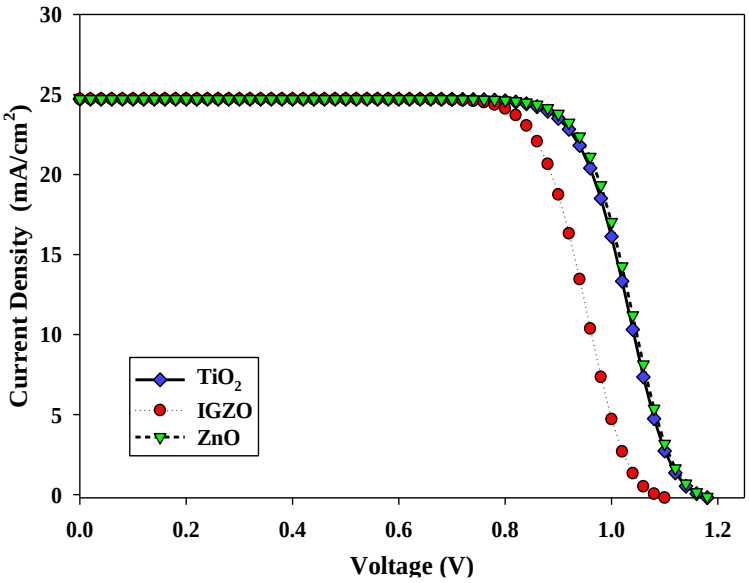

Fig. 2. J-V curves of PCs with TiO_2, IGZO, and ZnO NCTLs.

B. The impact of NCTL thickness on photovoltaic parameters of PCs

All three IGZO, TiO_2, and ZnO NCTLs were examined with thicknesses ranging from 30 to 400 nm. The V_{oc} of the cell remains unaffected by raising the thickness of the NCTLs. The J_{sc} experiences a minor decline as the thickness of the IGZO NCTL increases, primarily due to higher absorption losses within this layer. The optical losses increase slightly, and the FF decreases with thickness up to 100 nm because the series resistance increases slightly. It is also observed in the TiO_2 material that increasing the layer thickness from 30 to 50 nm slightly reduces the FF, lowering the efficiency. This decrease is due to the increased thickness of the TiO_2 layer, which reduces the electron mobility and increases the light reflection, resulting in less light absorption by the absorber layer. Fig. 3 shows that ZnO does not experience this issue as a result of its high electron mobility and conductivity. The thickness changes in this range have the least impact on it. On the other hand, as mentioned above, the TiO_2 processing process is costly, and the goal is to reduce cell costs. IGZO does not perform well and is also an expensive material. However, ZnO does not require high-temperature, high-cost processing and is an inorganic and inexpensive material. It also performs better than the other two materials. Therefore, in the remaining simulations, ZnO will be used.

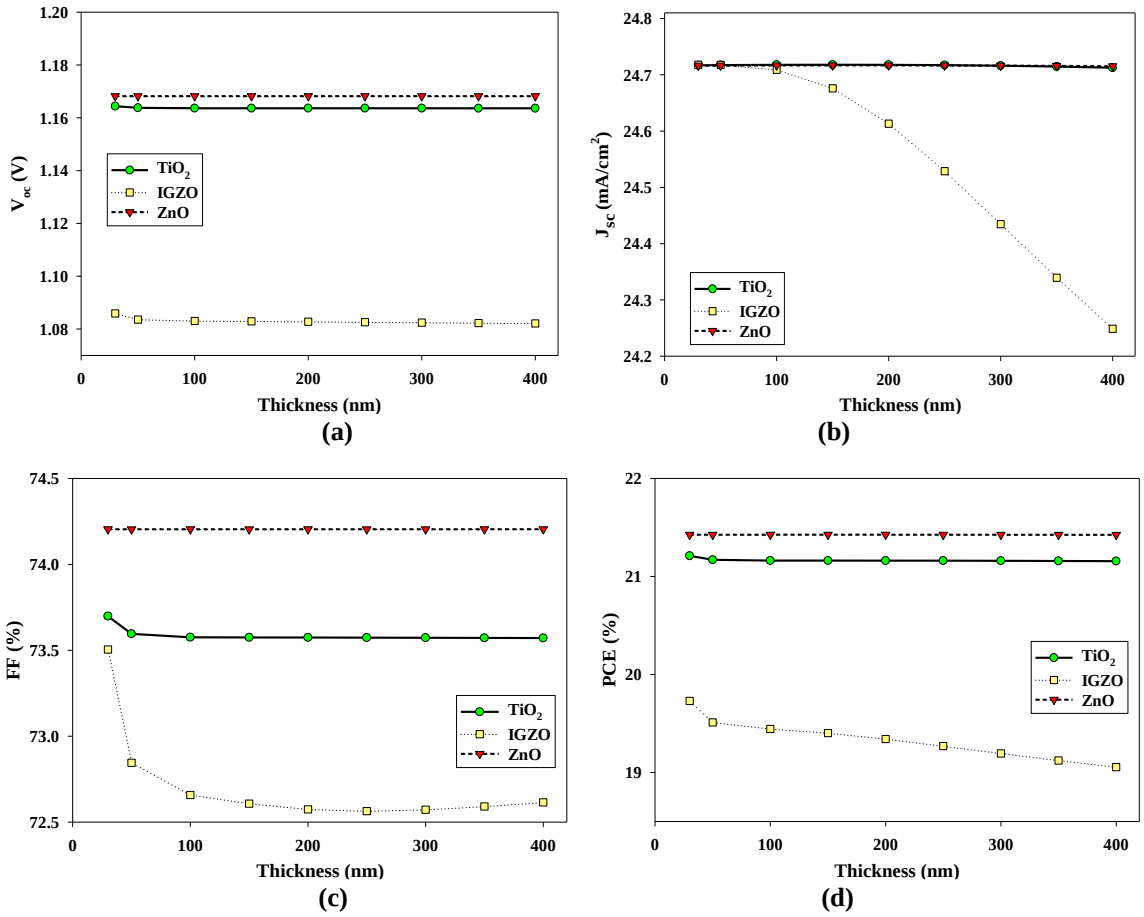

Fig. 3. The cell performance with TiO_2, IGZO, and ZnO NCTLs (a) V_{oc}, (b) J_{sc}, (c) FF, and (d) efficiency.

C. Efficiency of solar cell with ZnO NCTL and using different PCTLs

In a solar cell, energy level alignment (ELA) refers to the careful arrangement of the ELs of the various layers, particularly the absorber, NCTL, and PCTL, to optimize charge-carrier separation and collection efficiency. Fig. 4 shows the ELs of the substances employed in the perovskite cell structure. Ideally, the ELA should minimize the energy loss and the non-radiative recombination between the absorber layer and the CTLs. One way to achieve optimal energy level alignment is to create a spike-like band alignment at heterogeneous interfaces. In other words, in this situation, the conduction band minimum of the NCTL exceeds that of the absorber layer. Additionally, the valence band of the PCTL lies below that of the absorber layer. This creates an internal electric field that moves carriers away from interface surfaces and reduces recombination rates [37]. The efficient transfer of electrons and holes between layers is crucial for achieving a high-performance device.

The performance improvement achieved by the proposed device is largely attributed to optimized band alignment at the perovskite/transport layer interfaces. In particular, the conduction band offset (CBO) at the ZnO/$CH_3NH_3PbI_3$ interface and the valence band offset (VBO) at the $CH_3NH_3PbI_3$/CBTS interface were tuned to avoid unfavorable "cliff" configurations. A cliff-type alignment (negative offset) creates a downward step in the band edge that facilitates the flow of minority carriers towards the interface, thereby enhancing Shockley-Read-Hall recombination and reducing V_{oc} and FF. In contrast, a flat or small spike-type offset (slightly positive CBO or VBO) introduces a modest barrier that selectively blocks minority carriers while still allowing efficient extraction of majority carriers, thus suppressing interfacial recombination. The ZnO NCTL and CBTS PCTL exhibit near-ideal offsets with $CH_3NH_3PbI_3$, resulting in reduced recombination losses and contributing to the high simulated PCE of the optimized FTO/ZnO/$CH_3NH_3PbI_3$/CBTS/Ni structure.

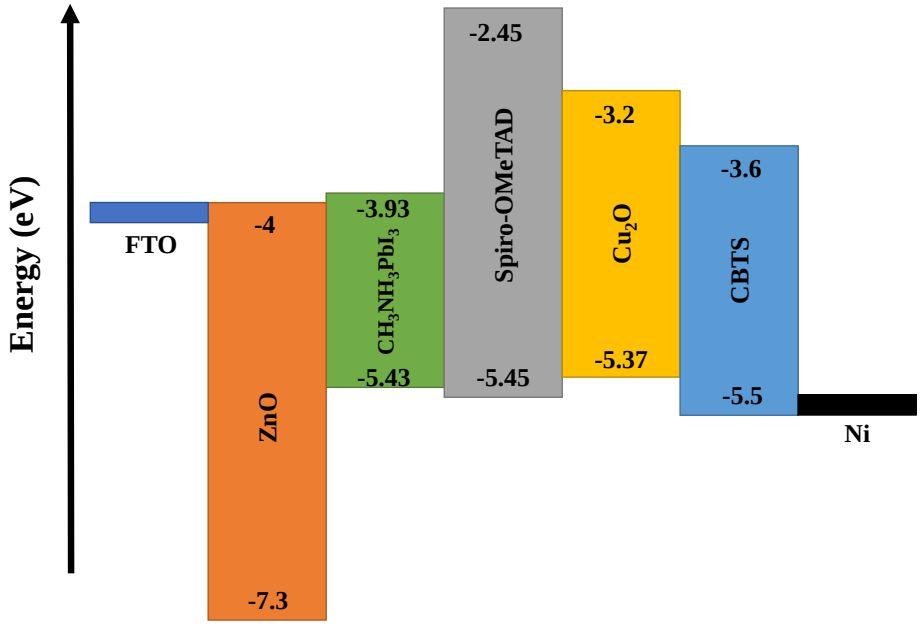

Fig. 4. Energy levels of the $CH_3NH_3PbI_3$ perovskite cell structure with different PCTLs.

The absorber layer is required to enable the transfer of the generated negative charge towards ZnO, while the PCTL guides holes towards the metal back contact. Fig. 5 and Table IV present the J-V curves and cell performance data for $CH_3NH_3PbI_3$ cells, which include ZnO with a thickness of 100 nm, as well as various PCTLs. Here, the thicknesses of the $CH_3NH_3PbI_3$ absorber layer and FTO are 450 nm and 500 nm, respectively. Based on the results, CBTS PCTL outperformed all other materials, attaining a V_{oc} of 1.16 V, a J_{sc} of 24.89 mA/cm^2, an FF of 84.98%, and a total efficiency of 24.75%. Cu_2O followed closely behind, with a V_{oc} of 1.16 V, a J_{sc} of 24.78 mA/cm^2, an FF of 84.89%, and a total efficiency of 24.55%. Spiro-OMeTAD, on the other hand, has an efficiency of 21.43%, which is lower than the others. It also obtained a V_{oc} of 1.16 V, a J_{sc} of 24.71 mA/cm^2, and an FF of 74.20%. Unlike other materials, Spiro-OMeTAD has lower efficiency and requires a hard and energy-intensive process to produce, making it less desirable for selection.

Overall, replacing the conventional TiO_2 and Spiro-OMeTAD charge-transport layers with ZnO and CBTS significantly improves the simulated performance of the $CH_3NH_3PbI_3$ perovskite solar cell. The optimized ZnO/CBTS configuration provides better band alignment at both interfaces, facilitating efficient carrier extraction and reducing recombination losses, resulting in a higher power conversion efficiency than the conventional TiO_2/Spiro-OMeTAD structure.

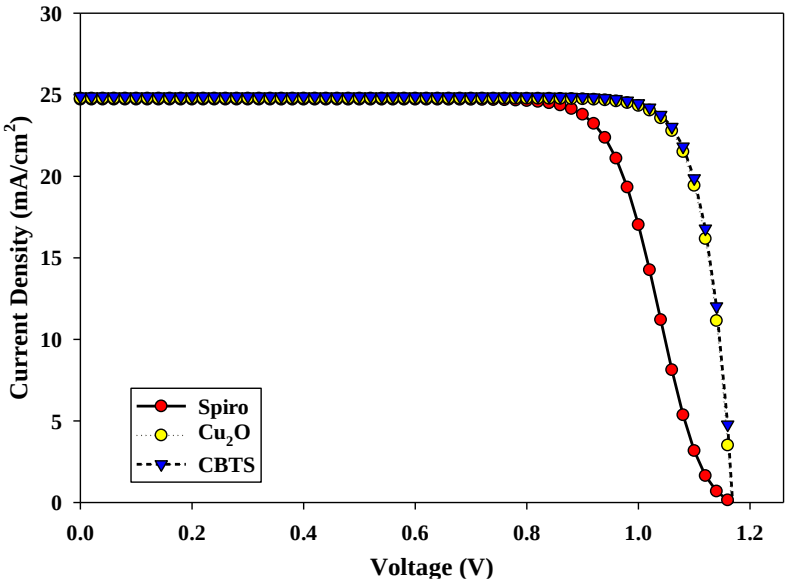

Fig. 5. J-V curves of PCs with Spiro-OMeTAD, Cu_2O, and CBTS as PCTLs.

TABLE IV
Output Parameters for Different PCTLs with 200 nm Thickness.

Device arrangement	V_{oc} (V)	J_{sc} (mA/cm^2)	FF (%)	PCE (%)
FTO/ZnO/$CH_3NH_3PbI_3$/Spiro-OMeTAD/Au	1.16	24.71	74.20	21.43
FTO/ZnO/$CH_3NH_3PbI_3$/Cu_2O /Au	1.16	24.78	84.89	24.55
FTO/ZnO/$CH_3NH_3PbI_3$/CBTS/Au	1.16	24.89	84.98	24.75

D. Effect of the thickness of the positive charge transport layer on solar cell performance

In this simulation, the ZnO thickness is 100 nm, and the PCTL thickness ranges from 50 to 300 nm. Fig. 6 shows the cell output parameters with three different PCTLs: Spiro-OMeTAD, Cu_2O, and CBTS.

The first notable point across all three materials is that increasing the thickness in this range does not have a considerable impact on increasing or decreasing the cell's V_{oc}, and, as mentioned earlier, the V_{oc} is mostly dependent on the bandgap and energy alignment of the layers. With increasing thickness, the J_{sc} of Spiro-OMeTAD has no tangible change, but the cell containing Cu_2O experiences a slight increase, as shown in Fig. 6b. Compared to the other two materials, the cell incorporating CBTS experiences a greater change in current density upon increasing the thickness, resulting in a slight boost in efficiency.

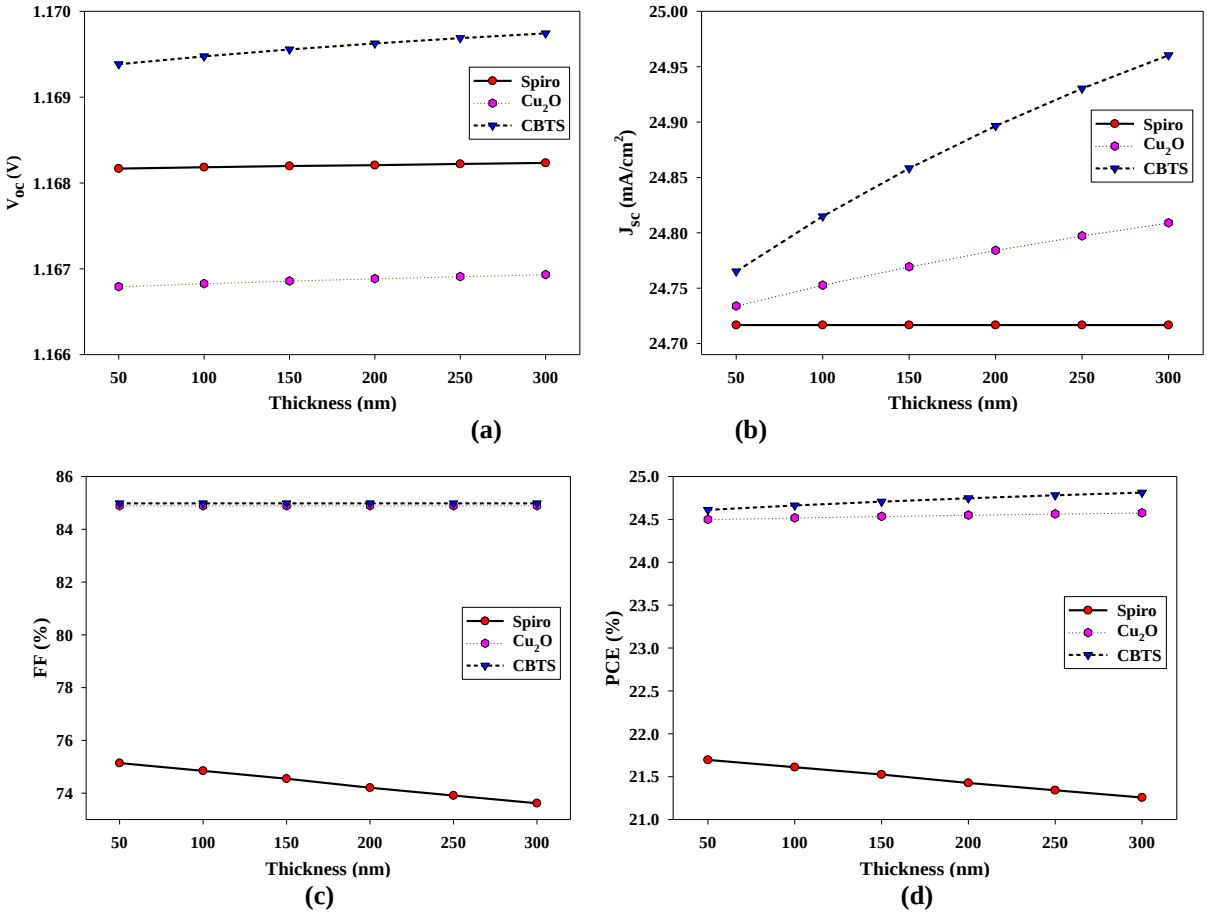

Fig. 6. Performance of the cell with Spiro-OMeTAD, Cu_2O, and CBTS PCTLs (a) V_{oc}, (b) J_{sc}, (c) FF, and (d) efficiency.

Increasing the thickness has a limited impact on the enhancement of FF and efficiency in cells containing CBTS and Cu_2O, primarily because of the increase in current density. It is noteworthy that, in general, the inorganic PCTLs exhibit high hole mobility and conductivity. The thickness changes have minimal effect, but increasing the Spiro-OMeTAD layer thickness significantly decreases the FF and the resulting efficiency. Considering this layer optimization, CBTS emerges as a promising material. Therefore, in the simulation, we will use CBTS as the PCTL.

E. The influence of the back electrode's work function on the ZnO/$CH_3NH_3PbI_3$/CBTS efficiency

Fig. 7 shows the changes in cell efficiency grounded on the

different back contacts (BCs). It is obvious from the information in Table V and Fig. 7 that copper (Cu) is not suitable for use as a metal back contact because of its low work function of 4.65 eV, which is much less than the energy balance required by the cell and the PCTL layer, which is about 5.5 eV. This causes a high recombination, a low V_{oc} of 0.96 V, and an FF of 69.60%. In general, elevating the work function increases efficiency and FF. The Schottky barrier effect is diminished due to the presence of high-work-function metals, leading to more efficient hole transmission [38]. Next, there is a carbon (C) with a 5 eV work function, which outperforms Cu and achieves an efficiency of 24.45%, but is still somewhat restricted by its low work function. The only advantage of carbon is its low price. Then gold (Au) with a 5.1 eV work function has a better profile. Gold is widely applied as an MBC due to its excellent conductivity in perovskite cells, and here it achieves 24.75% efficiency.

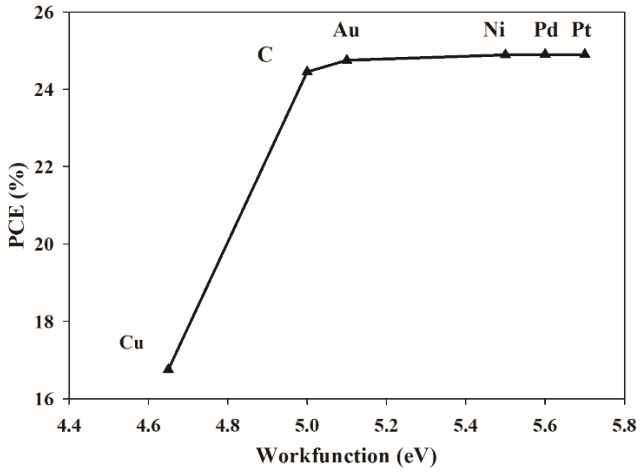

Fig. 7. The influence of various metal back contacts' work function on the perovskite cell efficiency, with $CH_3NH_3PbI_3$ absorber, ZnO as the NCTL, and CBTS as the PCTL.

TABLE V
Comparing cell Parameters Utilizing Various MBCs.

MBC	Work function (eV)	V_{oc} (V)	J_{sc} (mA/cm^2)	FF (%)	PCE (%)
Cu	4.65	0.96	24.89	69.60	16.75
C	5	1.16	24.89	83.95	24.45
Au	5.1	1.16	24.89	84.98	24.75
Ni	5.5	1.16	25.02	85.01	24.89
Pd	5.6	1.16	25.03	85.01	24.90
Pt	5.7	1.16	25.04	85.01	24.90

While gold (Au) offers a better profile than carbon, its high price and cost can limit its practicality for large-scale photovoltaic applications. Additionally, gold can experience difficulties in energy alignment with certain materials, further hindering its effectiveness. Nickel (Ni) with a 5.5 eV work function was then explored as an alternative, offering several advantages over Au. Ni has a better energy balance with the cell, making it a more effective choice for photovoltaic applications. The FF has been enhanced, accompanied by a slight decrease in the recombination rate, leading to an improvement in cell efficiency to 24.89% and thus showing a moderate overall improvement. Nickel is used in many experiments in perovskite cells. Nickel is also much more cost-effective than gold and has good conductivity. Finally, there are palladium (Pd) and platinum (Pt), both of which are highly efficient materials with work functions of 5.6 eV and 5.7 eV, individually. However, their relatively high cost limits their widespread adoption, despite their impressive 24.90% efficiency. On the other hand, the choice of PCTL thickness and the back metal electrode layer should be done more carefully to prevent recombination. Other studies also show that changing the back metal electrode alters the efficiency of the cell changes [13]. Due to the efficiency limitations of copper and carbon and the high cost of gold, palladium, and platinum, Nickel is chosen as the metal back contact within the cell, striking a balance between performance and affordability. Ni offers a cost-effective alternative, boasting suitable work function and functional properties, while still delivering a commendable efficiency.

F. Thickness optimization of the $CH_3NH_3PbI_3$ absorber layer

Figs. 8a and 8c show that increasing the $CH_3NH_3PbI_3$ layer

thickness results in a marginal decline in V_{oc} and a reduction in FF, owing to enhanced recombination. Conversely, Fig. 8b illustrates that increasing the thickness of the $CH_3NH_3PbI_3$ absorber enhances light absorption and carrier generation, thereby increasing the J_{sc}. However, excessively thick absorber layers increase carrier transport distance and the probability of bulk recombination, which may reduce charge collection efficiency and negatively affect the V_{oc} and FF. As depicted in Fig. 8b, beyond 900 nm, J_{sc} shows no notable increase, and the rate of increase diminishes incrementally. This stabilizes the cell efficiency at approximately 900 to 1000 nm, and from 1000 nm onward, the efficiency experiences a slight decline due to the greater influence of V_{oc} and FF relative to the marginal increase in J_{sc}, as illustrated in Fig. 8d. Hence, for the optimal thickness of the $CH_3NH_3PbI_3$ layer, a thickness of 900 nm is considered. In this thickness, the V_{oc} of 1.14 V, J_{sc} of 27.48 mA/cm^2, FF of 84.27%, and cell PCE of 26.38% are obtained.

Increasing the thickness of the $CH_3NH_3PbI_3$ absorber enhances light absorption and carrier generation, thereby increasing the short-circuit current density. However, excessively thick absorber layers increase carrier transport distance and the probability of bulk recombination, which may reduce charge collection efficiency and negatively affect the open-circuit voltage and fill factor.

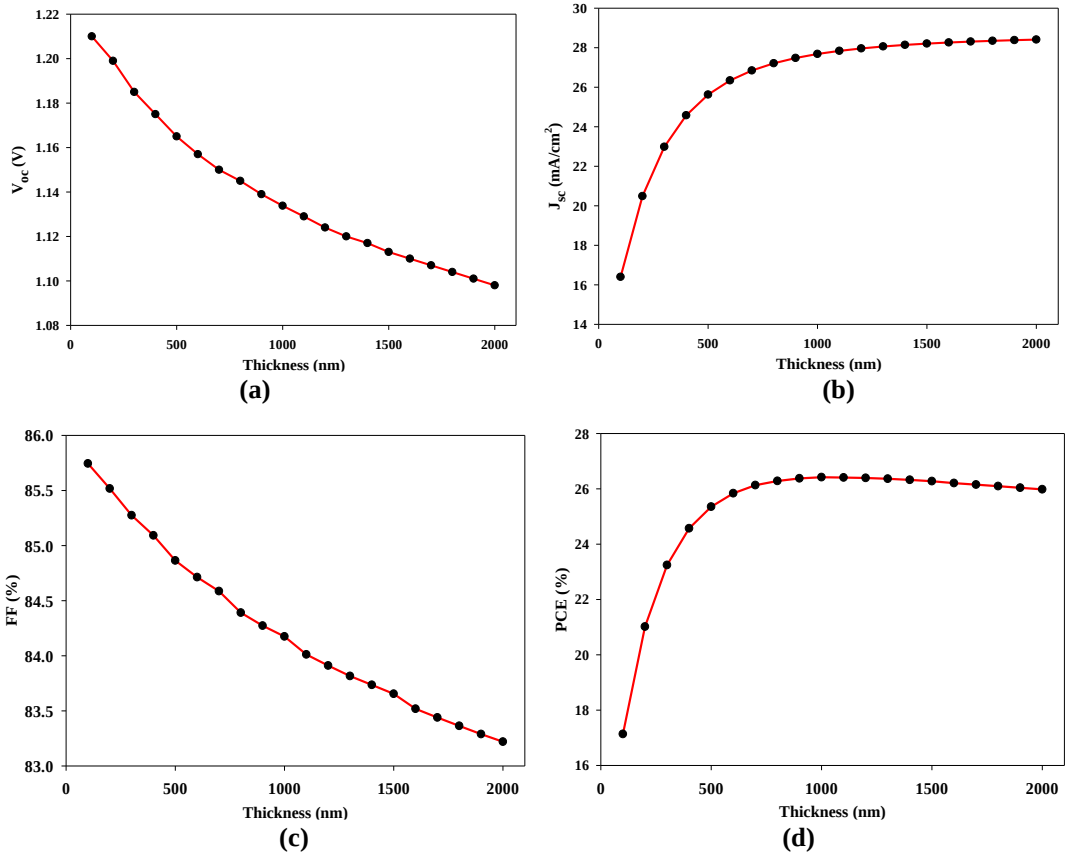

Fig. 8. Optimization of $CH_3NH_3PbI_3$ absorber layer Thickness from 100 to 2000 nm, (a) V_{oc}, (b) J_{sc}, (c) FF, and (d) efficiency.

G. Thickness optimization of the CBTS positive charge transport layer

As indicated in Fig. 9, the thickness of the CBTS hole-transport layer had only a minor influence on the simulated device performance. CBTS primarily serves as a hole-selective contact and does not contribute significantly to light absorption. Once the layer is thick enough to form a continuous film that provides efficient hole extraction and suppresses electron leakage, further increases in thickness have little effect on charge transport or recombination. Because CBTS exhibits relatively high hole mobility and moderate conductivity, variations within the studied range (50-300 nm) result in only slight changes in series resistance and electric field distribution. As a result, the key photovoltaic parameters remain nearly constant with increasing CBTS thickness, explaining the weak dependence of PCE observed in Fig. 9.

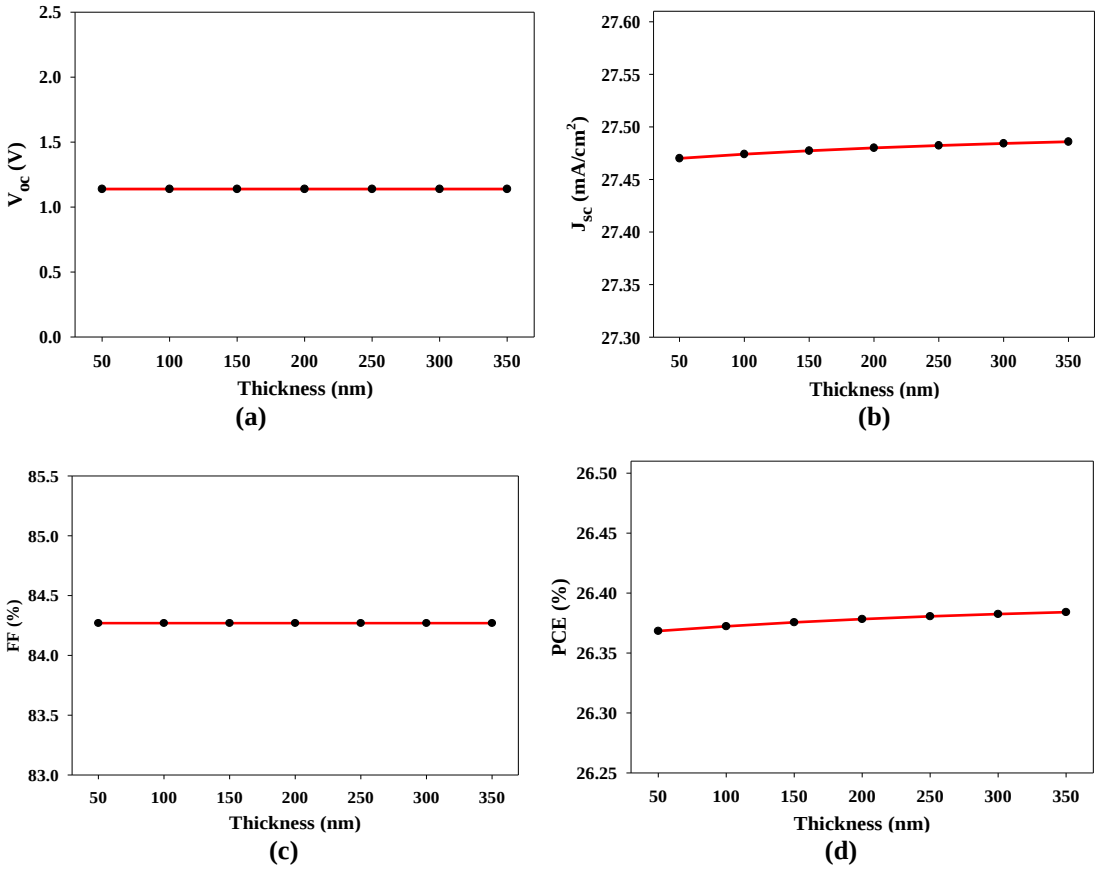

Fig. 9. Optimization of CBTS from 50 to 350 nm (a) V_{oc}, (b) J_{sc}, (c) FF, and (d) efficiency.

TABLE VI
Performance Characteristics of the FTO/ZnO/$CH_3NH_3PbI_3$/CBTS/Ni Perovskite Cell with Optimized CBTS layer.

Device arrangement	V_{oc} (V)	J_{sc} (mA/cm^2)	FF (%)	PCE (%)
FTO/ZnO/$CH_3NH_3PbI_3$/CBTS/Ni	1.14	27.48	84.27	26.38

Figs. 9a and 9c demonstrate that the V_{oc} and FF have remained unchanged, attributed to high hole mobility and conductivity, indicating that altering the thickness has little impact on these parameters. For this layer, a thickness of 200 nm is considered. In general, if the PCTL is set too thick, it may cause problems with hole transfer. So, the optimal thickness of 200 nm is chosen for the CBTS layer. Table VI finally presents the cell's outcome parameters after the CBTS PCTL thickness is fine-tuned.

H. Optimization of defect density in the absorber layer, and at ZnO/absorber and absorber/CBTS interfaces

The rise in defect density, which is tied to film quality, directly reduces cell efficiency by promoting recombination. The SRH recombination directly reduces lifetime and efficiency. Recombination of carriers is calculated based on Eq. (7) [38]:

$$R_{SRH} = \frac{\left[n_p - n_i \right]}{\left[\tau \times \left(p + n + \frac{2n_i \left(E_i - E_t \right)}{kT} \right) \right]} \quad (7)$$

$$\tau = \frac{1}{\delta \times N_t \times V_{th}} \quad (8)$$

In the above equations, δ denotes the capture cross-section that the negative and positive charges occupy, τ signifies the longevity of the negative and positive charges, and V_{th} denotes the charge carriers' thermal velocity. It is noteworthy that the number of defects in a perovskite crystal can be reduced by using the right coating conditions, improving its crystallinity, and reducing non-radiative recombination [39].

As shown in Figs. 10a and 10b, by enhancing the bulk defect density (N_t) of the $CH_3NH_3PbI_3$ layer from 7×10^{13} to 10^{18} cm^{-3},

the V_{oc} is greatly lowered, from 1.14 to 0.7 V. On the other hand, the J_{sc} was initially 27.48 mA/cm^2 and showed a very small reduction to the defect density of 10^{16} cm^{-3}. However, after this minor reduction, it has dropped sharply, reaching 22.28 mA/cm^2. As shown in Figs. 10c and 10d, the FF fell after defect density of 10^{14} cm^{-3} and went from 84.27% to 50.28%. Finally, cell efficiency has fallen sharply from 26.38% to 7.87%. According to Fig. 10, the optimal bulk defect density (N_t) is about 10^{14} cm^{-3}. Table VII illustrates the performance characteristics of the cell in optimal defect density conditions.

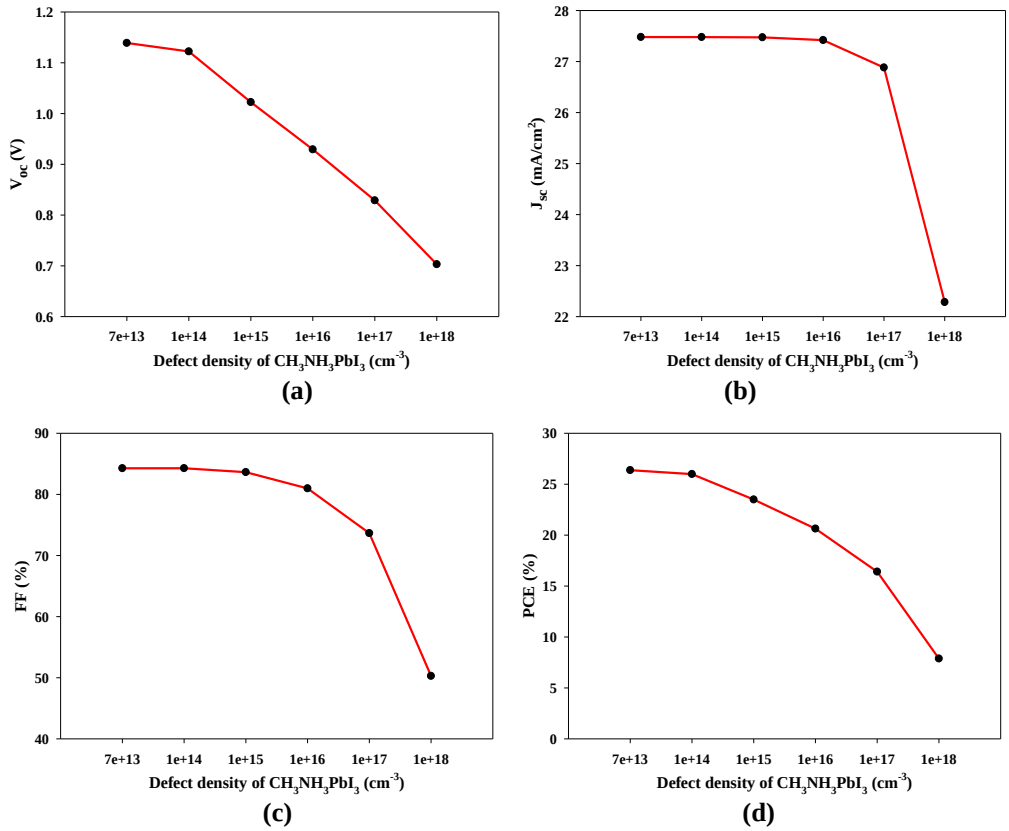

Fig. 10. Output parameters of the cell under optimization of defect density (N_t) $CH_3NH_3PbI_3$ layer: (a) V_{oc}, (b) J_{sc}, (c) FF, and (d) efficiency.

TABLE VII
Performance Characteristics of the ZnO/$CH_3NH_3PbI_3$/CBTS/Ni Cell with a BDD of 7×10^{13} cm^{-3}.

Device structure	V_{oc} (V)	J_{sc} (mA/cm^2)	FF (%)	PCE (%)
FTO/ZnO/$MAPbI_3$/CBTS/Ni	1.14	27.48	84.27	26.38

It is important to note that the optimum defect density of 7×10^{13} cm^{-3} used in the simulation represents an optimistic yet experimentally achievable value for high-quality $CH_3NH_3PbI_3$ films. Recent advances in solvent engineering, additive-assisted crystallization, and surface passivation have enabled perovskite layers with defect densities in the range of 10^{14}-10^{15} cm^{-3}, and in some cases approaching 10^{13} cm^{-3}. However, further reduction of bulk and interfacial defects is limited by intrinsic material properties, including ionic migration, dynamic defect formation, residual strain, grain boundary imperfections, and surface instabilities at perovskite/transport-layer interfaces. These factors impose a practical lower bound on achievable trap densities in real devices. Therefore, the defect density used in the simulation should be interpreted as a best-case scenario representative of high-quality perovskite films obtained under optimized fabrication conditions.

Fig. 11 illustrates how the efficiency of the $CH_3NH_3PbI_3$ cell is influenced by the defect density at the NCTL/$CH_3NH_3PbI_3$ and $CH_3NH_3PbI_3$/PCTL interfaces. The defect density at both interfaces is varied over a range of 1×10^{11} to 1×10^{15} cm^{-2}. Fig. 11 shows that within this range, as the defect density at the interfaces escalates, cell efficiency declines. Defects induce an elevated rate of carrier recombination at the interfaces.

Overall, the interface defect densities at the ZnO/$CH_3NH_3PbI_3$ and $CH_3NH_3PbI_3$/CBTS interfaces significantly influence carrier recombination and current transport. Higher interface defect densities introduce trap-assisted recombination centers that reduce carrier lifetime and hinder charge extraction, leading to a decline in J_{sc} and overall device performance. The ZnO/$CH_3NH_3PbI_3$ interface was found to be more sensitive to variations in defect density, indicating the importance of minimizing recombination at this junction to maintain efficient electron extraction.

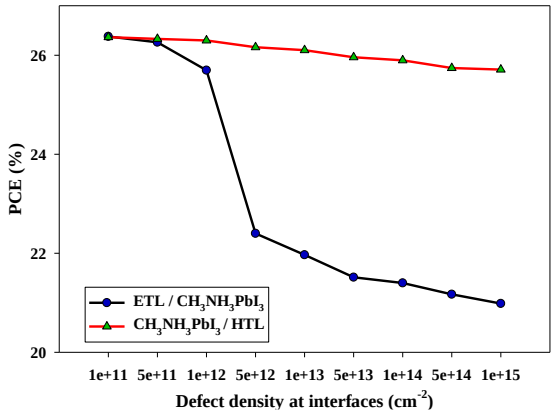

Fig. 11. The relationship between defect density at the NCTL/$CH_3NH_3PbI_3$ and $CH_3NH_3PbI_3$/PCTL interfaces and efficiency.

I. Influence of parasitic resistances on cell efficiency

The series resistance (R_s) of the cell significantly affects cell efficiency. The total R_s is shaped by the resistances within the individual layers, notably those integrated within the cell, the surface resistance, and the resistance at the semiconductor-electrode junctions. TCO is highly conductive and typically exhibits minimal increases in series resistance [40], thereby rendering the overall series resistance largely dictated by the material resistance and interface properties of the semiconductors and metals involved. R_S significantly affects FF, resulting in a reduction of the overall efficiency [41,42]. Fig. 12 indicates V_{oc} and J_{sc} remain approximately constant over the range of 0 to 6 Ωcm^2 as the series resistance increases. The FF has also decreased significantly from 84.27% to 71.08%. Eventually, cell efficiency declined significantly from 26.38% to 22.25% due to a significant reduction in FF.

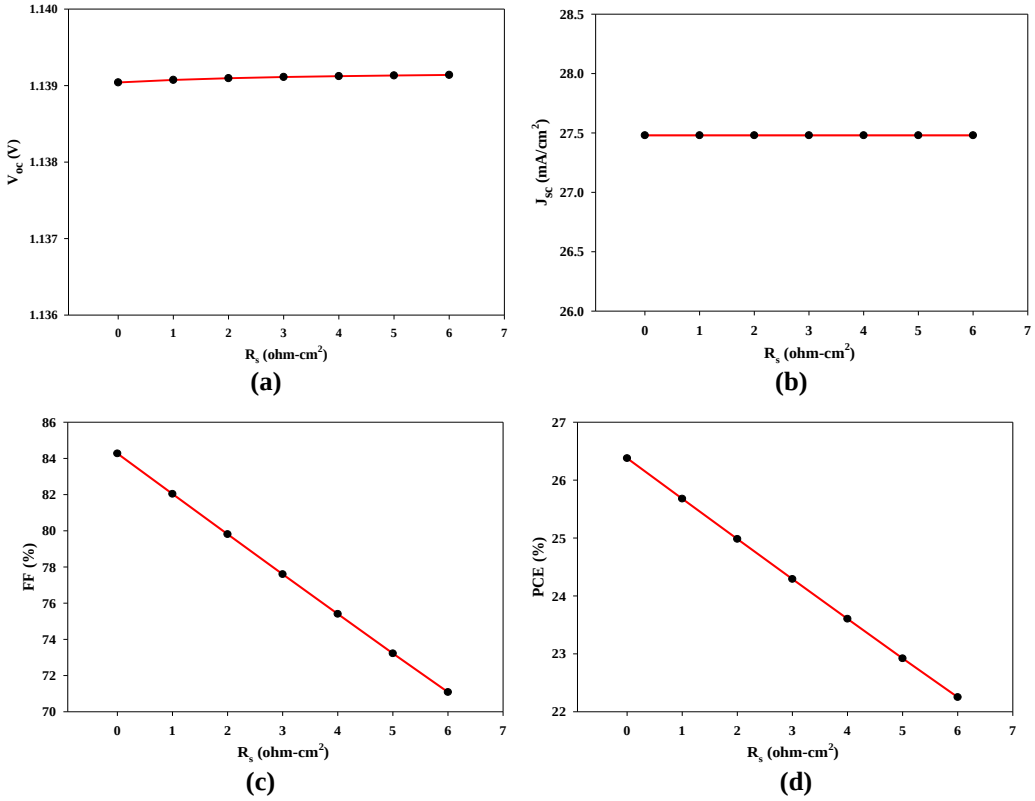

Fig. 12. Influence of R_s on photovoltaic parameters, (a) V_{oc}, (b) J_{sc}, (c) FF, and (d) efficiency.

Fig. 13 shows the influence of increasing shunt resistance (R_{sh}) from 10^1 to 10^7 Ωcm^2. As expected, the increase in R_{sh} has not affected the J_{sc}. As the R_{sh} resistance increased from 10 to 100 Ωcm^2, the V_{oc} increased correspondingly, rising from 0.27 to 1.11 V. Then, beyond 10^3 Ωcm^2, the V_{oc} remained constant at around 1.14 V. The FF has improved significantly, rising from 25% to 81.25% as the R_{sh} resistance varied from 10 to 1000 Ωcm^2. Beyond this point, the FF approached stability and eventually reached approximately 84.27%.

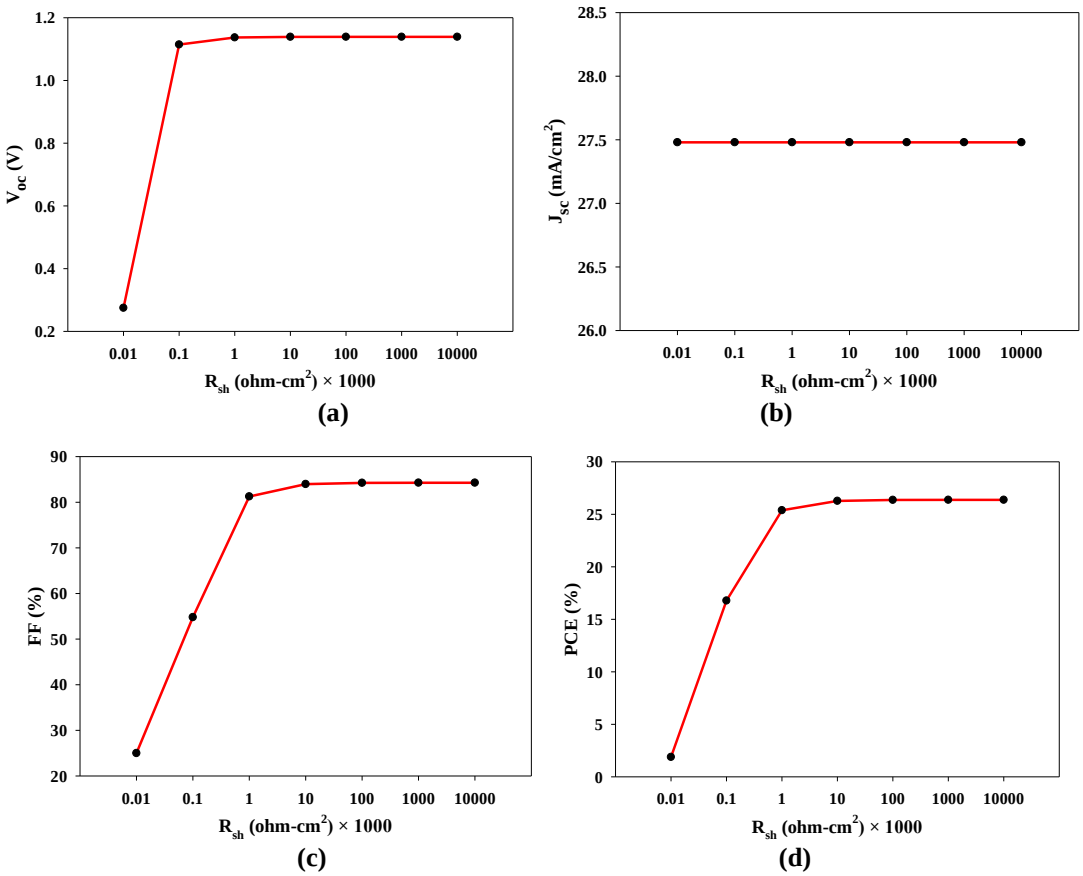

Fig. 13. Influence of R_{sh} on photovoltaic parameters (a) V_{oc}, (b) J_{sc}, (c) FF, and (d) efficiency.

Consequent to the augmentations in V_{oc} and FF, the efficiency also improved, rising from 1.88% at 10 Ωcm^2 to 25.38% at 1000 Ωcm^2. Beyond this point, efficiency increased more slowly, ultimately reaching 26.38%.

J. Influence of temperature on cell efficiency

The rise in cell temperature significantly impacts cell performance. As the temperature increases, the diffusion length expands, resulting in improved carrier mobility and subsequently, higher current density. However, a temperature rise also increases the recombination rate, thereby adversely influencing the V_{oc}, FF, and PCE [43,44].

Fig. 14 illustrates changes in cell parameters with temperature, ranging from 280 to 500 K. At 280 K, the V_{oc} of 1.17 V and the FF of 85.33% begin to decrease significantly. As the temperature continues to rise, the V_{oc} and FF decrease almost linearly, attaining values of 1.14 V and 84.28%, individually, at 300 K. Further increases in temperature result in a more pronounced decline in V_{oc} and FF, with values of 0.81 V and 72.29%, individually, achieved at 500 K. While the J_{sc} increases slightly with increasing temperature, the significant reduction in V_{oc} and FF indefinitely results in a diminution in the PCE of the cell. Specifically, the efficiency diminishes from 27.41% at 280 K to 16.25% at 500 K.

The degradation of device performance with increasing temperature can be attributed to several temperature-dependent physical mechanisms. As the temperature rises, the bandgap of the $CH_3NH_3PbI_3$ absorber slightly decreases due to bandgap narrowing, which reduces the open-circuit voltage according to the fundamental relation between bandgap energy and V_{oc}. In addition, higher temperatures increase carrier thermal energy and enhance Shockley-Read-Hall recombination in the absorber layer and at interfaces, which reduces carrier lifetime and increases recombination losses. Furthermore, the built-in potential across the junction decreases with temperature due to the temperature dependence of carrier concentrations and band energetics. The resulting reduction in the internal electric field weakens carrier separation and transport, leading to decreases in fill factor and overall power conversion efficiency. These combined effects explain the observed reduction in PCE at elevated operating temperatures shown in Fig. 14.

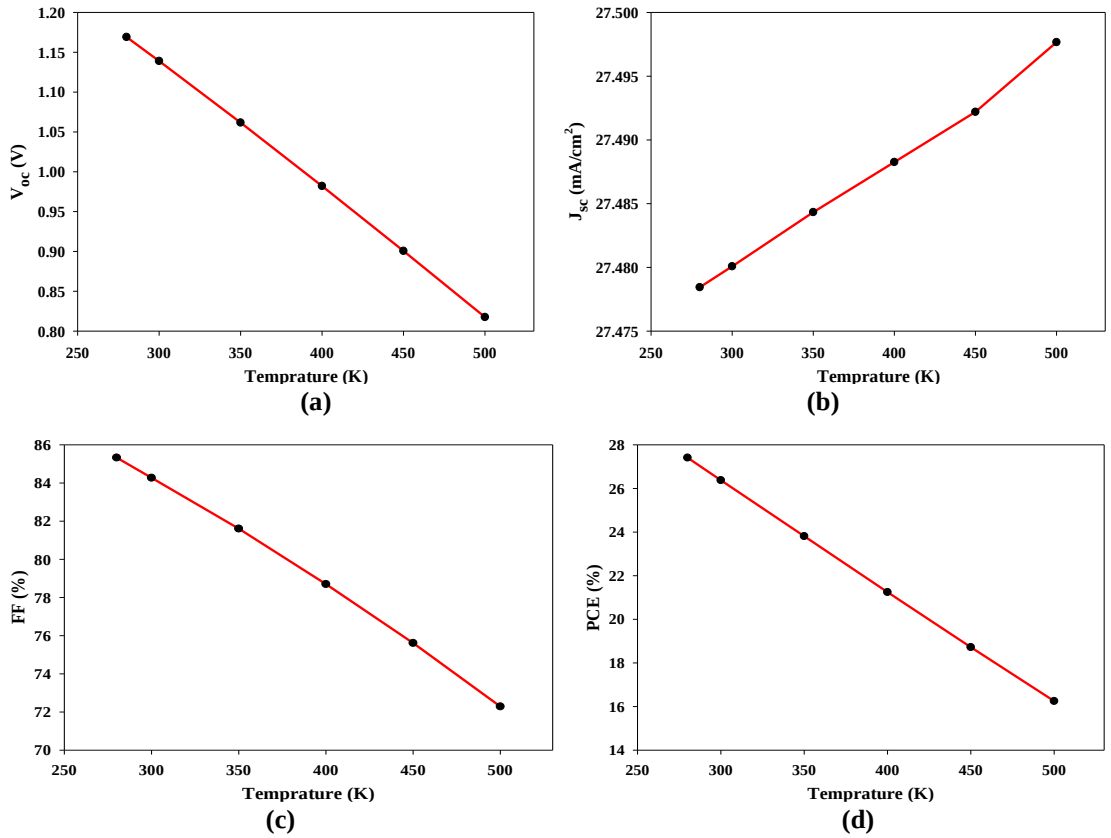

Fig. 14. Impact of temperature on photovoltaic parameters (a) V_{oc}, (b) J_{sc}, (c) FF, and (d) efficiency.

IV. Conclusion

This research aimed to improve the efficiency and reduce the cost of $CH_3NH_3PbI_3$-based PCs by employing a variety of positive charge-transport layers (PCTLs) and negative charge-transport layers (NCTLs). Initially, a cell with the configuration of FTO/NCTL/$CH_3NH_3PbI_3$/PCTL/Au was considered. The purpose of comparing and simulating different materials was to find the most efficient and suitable compounds and materials for NCTLs and PCTLs to increase cell efficiency. In the initial stage, we compared the performance of three NCTL materials at a fixed thickness of 100 nm. The materials were TiO_2, IGZO, and ZnO. Among the three, ZnO demonstrated the highest efficiency of 21.43%, followed by TiO_2 with 21.16% and IGZO with 19.44%. The findings suggest that ZnO could serve as a potent NCTL substance in solar cells. The PCTL also consisted of three materials, including one organic material, Spiro-OMeTAD, and two inorganic materials, Cu_2O and CBTS. After comparing the three structures at a fixed thickness of 200 nm for PCTL, it was determined that CBTS was the most suitable material, with an efficiency of 24.75%. Additionally, the effectiveness of these materials was assessed at varying thicknesses, with CBTS consistently delivering superior outcomes. Accordingly, a CBTS thickness of 200 nm was selected for the PCTL layer. Ni was also the most efficient metal back contact for this cell because it was more cost-effective than other materials such as Au, Pt, and Pd, and also had a suitable energy level. Then, the new arrangement composed of FTO/ZnO/$CH_3NH_3PbI_3$/CBTS/Ni was evaluated under layer thickness optimization to increase efficiency. For the validation and verification of the solar cells, the impacts of interface defect, Rs, Rsh, and temperature were also studied. In addition, the defect density of the $CH_3NH_3PbI_3$ layer was optimized, and finally, with a defect density of 7×10^{13} cm^{-3}, it achieved an efficiency of 26.38%, a V_{oc} of 1.14 V, a J_{sc} of 27.48 mA/cm^2, and a FF of 84.27%.

Authors Contribution

AGK: Conceptualization, Methodology, Software, Writing - original draft.

SMS: Validation, Investigation, Writing - review & editing, Supervision.

IGH: Software, Validation, Investigation, Writing - review & editing.

RK: Validation, Investigation, Writing - review & editing, Supervision.

Funding Statement

This research received no specific grant from any funding agency in the public, commercial, or not-for-profit sectors.

Conflicts of Interest

The author declares that there is no conflict of interest regarding the publication of this article.

Statement on the use of Generative AI

No AI-assisted technologies were used in the preparation of this manuscript.

REFERENCES

[1] N.A.N. Ouedraogo, G.O. Odunmbaku, Y. Ouyang, X. Xiong, B. Guo, S. Chen, S. Lu, K. Sun, Eco-friendly processing of perovskite solar cells in ambient air, Renew. Sust. Energy Rev. 192 (2024) 114161.

[2] H. Si, X. Zhao, Z. Zhang, Q. Liao, Y. Zhang, Low-temperature electron-transporting materials for perovskite solar cells: Fundamentals, progress, and outlook, Coord. Chem. Rev. 500 (2024) 215502.

[3] H. Lin, M. Yang, X. Ru, G. Wang, S. Yin, F. Peng, C. Hong, M. Qu, J. Lu, L. Fang, C. Han, P. Procel, O. Isabella, P. Gao, Z. Li, X. Xu, Silicon heterojunction solar cells with up to 26.81% efficiency achieved by electrically optimized nanocrystalline-silicon hole contact layers, Nat. Energy 8 (2023) 789-799.

[4] P.K. Patel, Device simulation of highly efficient eco-friendly CH3NH3SnI3 perovskite solar cell, Sci. Rep. 11 (2021) 3082.

[5] M.A. Green, E.D. Dunlop, M. Yoshita, N. Kopidakis, K. Bothe, G. Siefer, X. Hao, Solar cell efficiency tables (Version 63), Prog. Photovolt. Res. Appl. 32 (2024) 3-13.

[6] M.S.S. Basyoni, M.M. Salah, M. Mousa, A. Shaker, A. Zekry, M. Abouelatta, M.T. Alshammari, K.A. Al-Dhlan, C. Gontrand, On the Investigation of Interface Defects of Solar Cells: Lead-Based vs Lead-Free Perovskite, IEEE Access, 9 (2021) 130221-130232.

[7] J. Burschka, N. Pellet, S.-J. Moon, R. Humphry-Baker, P. Gao, M.K. Nazeeruddin, M. Grätzel, Sequential deposition as a route to high-performance perovskite-sensitized solar cells, Nature 499 (2013) 316-319.

[8] X. Guo, H. Dong, W. Li, N. Li, L. Wang, Multifunctional MgO Layer in Perovskite Solar Cells, ChemPhysChem. 16 (2015) 1727-1732.

[9] S.K. Pandey, S. Somay, Device Engineering Approach Toward Stable, Efficient, and Eco-Friendly Perovskite Solar Cell, IEEE Trans. Electron Devices 68 (2021) 1142-1148.

[10] D. Liu, J.K. Smith, Inflation forecasts and core inflation measures: Where is the information on future inflation?, Q. Rev. Econ. Finance 54 (2014) 133-137.

[11] N. Rono, A.E. Merad, J.K. Kibet, B.S. Martincigh, V.O. Nyamori, Simulation of the photovoltaic performance of a perovskite solar cell based on methylammonium lead iodide, Opt. Quantum Electron. 54 (2022) 317.

[12] F. Azri, A. Meftah, N. Sengouga, A. Meftah, Electron and hole transport layers optimization by numerical simulation of a perovskite solar cell, Sol. Energy 181 (2019) 372-378.

[13] Y. Raoui, H. Ez-Zahraouy, N. Tahiri, O. El Bounagui, S. Ahmad, S. Kazim, Performance analysis of MAPbI3 based perovskite solar cells employing diverse charge selective contacts: Simulation study, Sol. Energy 193 (2019) 948-955.

[14] W. Yu, F. Li, H. Wang, E. Alarousu, Y. Chen, B. Lin, L. Wang, M.N. Hedhili, Y. Li, K. Wu, X. Wang, O.F. Mohammed, T. Wu, Ultrathin Cu2O as an efficient inorganic hole transporting material for perovskite solar cells, Nanoscale 8 (2016) 6173-6179.

[15] M.K. Hossain, G.F.I. Toki, I. Alam, R. Pandey, D.P. Samajdar, M.F. Rahman, M.R. Islam, M.H.K. Rubel, H. Bencherif, J. Madan, M.K.A. Mohammed, Numerical simulation and optimization of a CsPbI3-based perovskite solar cell to enhance the power conversion efficiency, New J. Chem. 47 (2023) 4801-4817.

[16] M. Burgelman, P. Nollet, S. Degrave, Modelling polycrystalline semiconductor solar cells, Thin Solid Films 361-362 (2000) 527-532.

[17] I. Gharibshahian, A.A. Orouji, S. Sharbati, Effectiveness of band discontinuities between CIGS absorber and copper-based hole transport layer in limiting recombination at the back contact, Mater. Today Commun. 33 (2022) 104220.

[18] F.S. Ahmadpanah, A.A. Orouji, I. Gharibshahian, Improving the efficiency of CIGS solar cells using an optimized p-type CZTSSe electron reflector layer, J. Mater. Sci. Mater. Electron. 32 (2021) 22535-22547.

[19] F. Ghamsari-Yazdel, I. Gharibshahian, S. Sharbati, Thin oxide buffer layers for avoiding leaks in CIGS solar cells; a theoretical analysis, J. Mater. Sci. Mater. Electron. 32 (2021) 7598-7608.

[20] I. Gharibshahian, S. Sharbati, A.A. Orouji, Potential efficiency improvement of Cu (In, Ga) Se2 thin-film solar cells by the window layer optimization, Thin Solid Films 655 (2018) 95-104.

[21] S. Sharbati, I. Gharibshahian, A.A. Orouji, Proposed suitable electron reflector layer materials for thin-film CuIn1−xGaxSe2 solar cells, Opt. Mater. 75 (2018) 216-223.

[22] I. Ahmad, K. Hayat, M. Ashraf, M. Imran, S.K. Shah, SCAPS-based simulation analysis of device parameters of ZnO-inverted polymer solar cells, Opt. Quantum Electron. 55 (2023) 345.

[23] S.K. Behura, S. Nayak, I. Mukhopadhyay, O. Jani, Junction characteristics of chemically-derived graphene/p-Si heterojunction solar cell, Carbon 67 (2014) 766-774.

[24] V. Rondan-Gómez, F. Ayala-Mató, D. Seuret-Jiménez, G. Santana-Rodríguez, A. Zamudio-Lara, I. Montoya De Los Santos, H.Y. Seuret-Hernández, New architecture in dye-sensitized solar cells: a SCAPS-1D simulation study, Opt. Quantum Electron. 52 (2020) 324.

[25] F. Jahantigh, M.J. Safikhani, The effect of HTM on the performance of solid-state dye-sanitized solar cells (SDSSCs): a SCAPS-1D simulation study, Appl. Phys. A 125 (2019) 276.

[26] D. Madadi, I. Gharibshahian, A.A. Orouji, High-performance α-FAPbI3 perovskite solar cells with an optimized interface energy band alignment by a Zn(O, S) electron transport layer, J. Mater. Sci. Mater. Electron. 34 (2023) 51.

[27] H. Jalali, A.A. Orouji, I. Gharibshahian, Controlled conduction band offset in Sb2Se3 solar cell through introduction of (Zn, Sn)O buffer layer to improve photovoltaic performance: A simulation study, Sol. Energy Mater. Sol. Cells 260 (2023) 112492.

[28] I. Gharibshahian, A.A. Orouji, S. Sharbati, An Analytical Model for Sb2Se3 Thin-Film Solar Cells by Considering Current-Voltage Distortion, Adv. Theory Simul. 6 (2023) 2200438.

[29] I. Gharibshahian, A.A. Orouji, S. Sharbati, Efficient Sb2(S, Se)3/Zn(O, S) solar cells with high open-circuit voltage by controlling sulfur content in the absorber-buffer layers, Sol. Energy 227 (2021) 606-615.

[30] I. Gharibshahian, A.A. Orouji, S. Sharbati, Effect of the junction barrier on current–voltage distortions in the Sb2Se3/Zn(O, S) solar cells, Opt. Mater. 116 (2021) 111098.

[31] I. Gharibshahian, A.A. Orouji, S. Sharbati, Towards high-efficiency Cd-Free Sb2Se3 solar cells by the band alignment optimization, Sol. Energy Mater. Sol. Cells 212 (2020) 110581.

[32] I. Gharibshahian, A.A. Orouji, S. Sharbati, Alternative buffer layers in Sb2Se3 thin-film solar cells to reduce open-circuit voltage offset, Sol. Energy 202 (2020) 294-303.

[33] C. Qiu, Y. Wu, J. Song, W. Wang, Z. Li, Efficient Planar Perovskite Solar Cells with ZnO Electron Transport Layer, Coat. 12 (2022) 1981.

[34] J.-X. Song, X.-X. Yin, Z.-F. Li, Y.-W. Li, Low-temperature-processed metal oxide electron transport layers for efficient planar perovskite solar cells, Rare Met. 40 (2021) 2730-2746.

[35] W. Zhong Lin, Zinc oxide nanostructures: growth, properties and applications, J. Phys. Condens. Matter 16 (2004) R829.

[36] J. Luo, Y. Wang, Q. Zhang, Progress in perovskite solar cells based on ZnO nanostructures, Sol. Energy 163 (2018) 289-306.

[37] J. Zhang, R. Chen, Y. Wu, M. Shang, Z. Zeng, Y. Zhang, Y. Zhu, L. Han, Extrinsic Movable Ions in MAPbI3 Modulate Energy Band Alignment in Perovskite Solar Cells, Adv. Energy Mater. 8 (2018) 1701981.

[38] I. Alam, R. Mollick, M.A. Ashraf, Numerical simulation of Cs2AgBiBr6-based perovskite solar cell with ZnO nanorod and P3HT as the charge transport layers, Phys. B: Condens. Matter 618 (2021) 413187.

[39] L. Lin, L. Jiang, P. Li, B. Fan, Y. Qiu, A modeled perovskite solar cell structure with a Cu2O hole-transporting layer enabling over 20% efficiency by low-cost low-temperature processing, J. Phys. Chem. Solids 124 (2019) 205-211.

[40] A. Bosio, S. Pasini, N. Romeo, The History of Photovoltaics with Emphasis on CdTe Solar Cells and Modules, Coat. 10 (2020) 344.

[41] M.K. Hossain, M.H.K. Rubel, G.F.I. Toki, I. Alam, M.F. Rahman, H. Bencherif, Effect of Various Electron and Hole Transport Layers on the Performance of CsPbI3-Based Perovskite Solar Cells: A Numerical Investigation in DFT, SCAPS-1D, and wxAMPS Frameworks, ACS Omega 7 (2022) 43210-43230.

[42] D. Jayan K, V. Sebastian, J. Kurian, Simulation and optimization studies on CsPbI3 based inorganic perovskite solar cells, Sol. Energy 221 (2021) 99-108.

[43] F. Behrouznejad, S. Shahbazi, N. Taghavinia, H.-P. Wu, E. Wei-Guang Diau, A study on utilizing different metals as the back contact of CH3NH3PbI3 perovskite solar cells, J. Mater. Chem. A 4 (2016) 13488-13498.

[44] S.R. Raga, E.M. Barea, F. Fabregat-Santiago, Analysis of the Origin of Open Circuit Voltage in Dye Solar Cells, J. Phys. Chem. Lett. 3 (2012) 1629-1634.